


Molecular dynamics study of the sonic horizon of microscopic Laval nozzlesHelmut Ortmayer^{1,2} and Robert E. Zillich¹¹*Institute for Theoretical Physics, Johannes Kepler University, 4040 Linz, Austria*²*Primetals Technologies (Austria) GmbH, A-4031 Linz, Austria* (Received 3 July 2023; revised 19 April 2024; accepted 13 May 2024; published 11 June 2024)

A Laval nozzle can accelerate expanding gas above supersonic velocities, while cooling the gas in the process. This work investigates this process for microscopic Laval nozzles by means of nonequilibrium molecular dynamics simulations of stationary flow, using grand-canonical Monte Carlo particle reservoirs. We study the steady-state expansion of a simple fluid, a monoatomic gas interacting via a Lennard-Jones potential, through an idealized nozzle with atomically smooth walls. We obtain the thermodynamic state variables pressure, density, and temperature but also the Knudsen number, speed of sound, velocity, and the corresponding Mach number of the expanding gas for nozzles of different sizes. We find that the temperature is well defined in the sense that the each velocity components of the particles obey the Maxwell-Boltzmann distribution, but it is anisotropic, especially for small nozzles. The velocity autocorrelation function reveals a tendency towards condensation of the cooled supersonic gas, although the nozzles are too small for the formation of clusters. Overall we find that microscopic nozzles act qualitatively like macroscopic nozzles in that the particles are accelerated to supersonic speeds while their thermal motion relative to the stationary flow is cooled. We find that, like macroscopic Laval nozzles, microscopic nozzles also exhibit a sonic horizon, which is well defined on a microscopic scale. The sonic horizon is positioned only slightly further downstream compared to isentropic expansion through macroscopic nozzles, where it is situated in the most narrow part. We analyze the sonic horizon by studying space-time density correlations, i.e., how thermal fluctuations at two positions of the gas density are correlated in time and find that after the sonic horizon there are indeed no upstream correlations on a microscopic scale.

DOI: [10.1103/PhysRevE.109.065104](https://doi.org/10.1103/PhysRevE.109.065104)**I. INTRODUCTION**

The Laval nozzle converts thermal kinetic energy into translational kinetic energy and was invented by Gustaf de Laval in 1888 for actuating steam turbines with steam accelerated by expansion. The goal was to achieve the highest possible velocity of an expanding gas, made possible with the convergent-divergent nozzle shape. The left panel of Fig. 1 schematically shows the cross section of such a nozzle. When the gas reaches the most narrow part, the nozzle throat, the flow can become supersonic. The surface where this happens is called sonic horizon (or acoustic horizon) [1,2] because no information carried by sound waves can travel upstream through the sonic horizon.

The expansion of gas in a Laval nozzle has interesting thermodynamic properties. While the gas acceleration of macroscopic Laval nozzles is exploited for propulsion purposes in rocket engines, the temperature drop during expansion through a nozzle with a diameter in the tenth of the micrometer range is exploited in supersonic jet spectroscopy to freeze out translational, rotational and vibrational degrees of freedom of molecules, leading to spectra that are not complicated by too many thermally populated excited states [3–6]. The studied molecules can be kept in a supercooled gas phase, far below the condensation temperature, with a high density compared to a conventionally cooled equilibrium vapor. Under appropriate conditions, weakly bound van der Waals cluster can be formed [7,8]. The molecules of interest are typically coexpanded with a noble gas. In case of ⁴He

as carrier the cooling effect is also greatly enhanced by the unique quantum effects of ⁴He at low temperatures. Especially the helium-droplet beam technique takes additional advantage from the superfluidity of ⁴He [7–9]. The typical orifice used for molecular beams has only a convergent part and the divergent nozzle part is realized by the ambient pressure in the expansion chamber. During expansion the surrounding gas in the chamber provides a pressure boundary to the jet and the jet temperature itself keeps decreasing after exiting the orifice [10].

Macroscopic Laval nozzles are well understood and can be approximately described by simple thermodynamic considerations, under assumptions that are reasonable for macroscopic nozzles: isentropic flow without dissipation (inviscid gas and smooth slip boundaries); the flow velocity v depends only on the position x along the axis of the nozzle; the nozzles cross section varies only gradually with x ; the flow is stationary; and continuum fluid dynamics is valid, i.e., each fluid element is in local thermodynamic equilibrium. Then the relative velocity change with x and the relative change of the cross-section area A follow the simple relation [10]

$$\frac{dv}{v} = -\frac{1}{1 - \left(\frac{v}{c}\right)^2} \frac{dA}{A}, \quad (1)$$

where c is the speed of sound, which can be expressed in terms of the isentropic or isothermic derivative of the pressure with

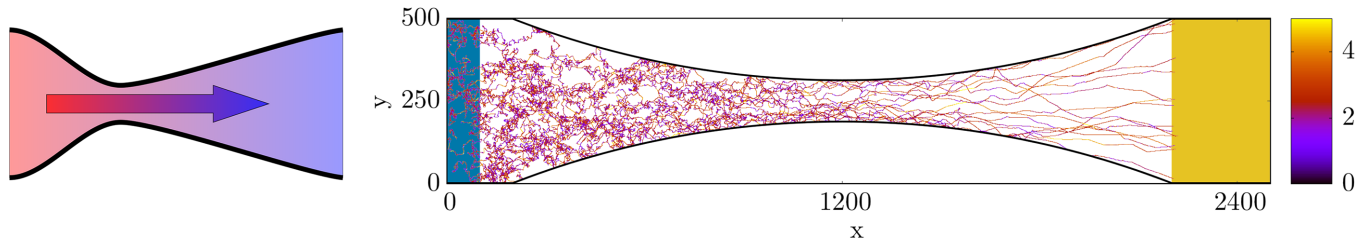


FIG. 1. Left: Cross section of a Laval nozzle with a convergent and divergent nozzle part. Indicated by the arrow and color is the flow direction and temperature decrease of the expanding gas. Right: Molecular dynamics trajectories of 30 randomly chosen particles starting in the shaded area to the left. The average total particle number in the nozzle for this simulation is much larger, approximately 790 000. The velocity of these particles is indicated by color. While the subsonic motion in the convergent part is dominated by random thermal motion, the supersonic motion of the particles in the divergent part is dominated by the flow velocity.

respect to the density,

$$c = \sqrt{\left(\frac{\partial p}{\partial \rho}\right)_S} = \sqrt{\frac{c_p}{c_v} \left(\frac{\partial p}{\partial \rho}\right)_T}, \quad (2)$$

where c_p and c_v is the heat capacity at constant pressure and volume, respectively. The ratio $M = v/c$ is called Mach number, and $M = 1$ defines the sonic horizon. The usual situation is a gas in a reservoir or a combustion chamber producing gas to the left in our figures of the nozzle. Hence the flow velocity is small when it enters the nozzle, in particular it is subsonic, $M < 1$. Equation (1) tells us that, with decreasing cross section A (e.g., moving downstream in the convergent part), the flow velocity v must increase. In the nozzle throat, i.e., where A has a minimum and $dA = 0$, v either stays below M , in which case v must decelerate in the divergent part. Or the gas flow attains $M = 1$ in the nozzle throat and then accelerates further in the divergent part (if the pressure difference between inlet and outlet is large enough). Hence for supersonic flow, v increases with *increasing* A . Note that Eq. (1) implies that the transition to supersonic flow can happen only where the cross-section area has a minimum.

The goal of this work is to understand the physics of microscopic Laval nozzles on the nanoscale of the atoms of the gas flowing through a constriction which is only nanometers wide. We want to answer the following questions: How do the transport properties of a Laval nozzle depend on its size, and does it even have the typical characteristic of a convergent-divergent nozzle, i.e., converting thermal energy into translational energy? If yes, then how efficiently does a nanoscale Laval nozzle cool the expanding gas? Do we obtain supersonic flow? Is there a well-defined sonic horizon, and if yes, then where in the nozzle is it located? Is there even local thermodynamic equilibrium such that we can define a local speed of sound and thus can speak of a sonic horizon and supersonic flow? Since we are interested in the fundamental mechanism of a microscopic Laval nozzle, we study a rather idealized nozzle with atomically flat surfaces corresponding to slip boundaries. This simplifies the problem since it eliminates the boundary layer close to the nozzle walls. Boundary effects are of course essential in a real microscopic nozzle, and they would be easy to model with rough walls, but they would complicate the analysis and interpretation of our results.

A common method to study microscopic nozzles is the direct simulation Monte Carlo (DSMC) method [11–14], which

solves the Boltzmann equation. However, we want to make as few approximations as possible, apart from the idealization of an atomically smooth nozzle walls. Therefore, we use molecular dynamics (MD) simulations, which account for each atom or molecule of the gas, and collisions are described by realistic intermolecular interactions. Atomistic (MD) simulations have been shown to be useful for the understanding of fluid dynamic phenomena [15–22]. The only underlying assumption of the MD method is that quantum physics plays no role and classical mechanics is sufficient. This is usually a valid assumption, with the exception of expansion of ^4He under conditions where the ^4He gas cools to superfluid nanodroplets [23].

Because of the nonequilibrium nature of this expansion process through a Laval nozzle we perform nonequilibrium MD (NEMD) simulations [24]. The right panel of Fig. 1 shows the trajectories for 30 randomly chosen particles of a simulation in a convergent-divergent nozzle that contained on average about 790 000 particles. The speed of the particles is color coded. Figure 1 gives an impression how a Laval nozzle converts thermal energy (temperature) to ordered translation energy: Close to the inlet, the motion is predominantly thermal; close to the outlet the velocities are higher and tend to point in x direction, but the temperature, i.e., the kinetic energy after subtracting the flow velocity, is in fact much lower as our results will show. Averaging over all particles and over time leads to the thermodynamic notion of a gas that accelerates and cools as it expands through the nozzle.

With MD we can obtain, with microscopic resolution, both thermodynamic quantities like temperature, pressure, or density, and microscopic quantities like the velocity autocorrelation function VACF, velocity distribution, or density fluctuation correlations: We will investigate whether the expanding gas has a well-defined temperature, characterized by an isotropic Maxwell-Boltzmann distribution of the thermal particle velocities. The VACF exhibits features related to the metastability of the accelerated gas cooled below condensation temperature. We calculate spatiotemporal density autocorrelations, i.e., correlations between fluctuations of the density at different times and different locations, to study the propagation of information upstream and downstream and pinpoint the location of the sonic horizon (if it exists). In a macroscopic nozzle, upstream propagation of information carried by density fluctuations is not possible in the supersonic region. On the microscopic scale, e.g., on the scale of the mean

free path of the atoms, a unidirectional information flow is not so obvious. For instance, if we assume a Maxwell-Boltzmann distribution of random particle velocities, then fast particles from the tail of the distribution could carry information upstream.

We remark that, in a seminal paper by W. G. Unruh *et al.* [1], a mathematical analog between the black hole evaporation by Hawking radiation and the fluid mechanical description of a sonic horizon is found. This analog has brought significant attention to sonic horizons [2,25–28], but in this work we will not study analog Hawking radiation.

II. MOLECULAR DYNAMICS SIMULATION OF EXPANSION IN LAVAL NOZZLE

The gas flow through the microscopic Laval nozzle is simulated with the MD method which solves Newton's equation of motion for all particles of the gas. Unlike in continuum fluid dynamics, which solves the Navier-Stokes equation, MD contains thermal fluctuations of the pressure and density, also in equilibrium. Furthermore, unlike the continuum description, MD does not assume local thermodynamic equilibrium, which may not be fulfilled in a microscopic nozzle.

The price for an accurate atomistic description afforded by MD simulations is a high computational cost compared to Navier-Stokes calculations or DSMC simulations. In the present case, we simulate up to several hundred thousand particles. Larger MD simulations are possible, but our focus is the microscopic limit of a Laval nozzles on the nanometer scale. A challenge for MD is to implement effective reservoirs to maintain a pressure differential for a steady flow between inlet and outlet of the nozzle. An actual reservoir large enough to maintain its thermodynamic state during the MD simulation would be prohibitively computationally expensive. We approximate these reservoirs by defining small inlet and outlet regions where we perform a hybrid MD and GC Monte Carlo simulation (GCMC) [29], with grand-canonical Monte Carlo exchange of particles [30]. As the name implies, this method simulates a grand-canonical ensemble for a given chemical potential μ , volume V , and temperature T by inserting and removing particles if the volume is closed. Since inlet and outlet regions are open to the nozzle region, the outflow and inflow of particles leads to a significant deviation from an equilibrium ensemble, even if the simulations reaches a steady flow state, as discussed below. The nozzle region itself is simulated without thermostat nor Monte Carlo exchange. This would correspond to the microcanonical ensemble at constant number of particles N , volume V , and energy E if the nozzle region were not open to the inlet and outlet regions. The nozzle walls are thermally insulating.

Figure 2 shows the geometry of the nozzle simulated with the inlet and outlet colored in blue and yellow, respectively, with the convergent-divergent nozzle in between. To keep the simulation simple and the computational effort in check we simulate a slit Laval nozzle, translationally invariant in z direction (perpendicular to the plane of the figure) and realized with periodic boundaries in this direction. Since our focus is a microscopic understanding of supersonic flow and the sonic horizon, we simulate a nozzle with atomically smooth walls, shown as thick black curved lines in Fig. 2. Simulating rough

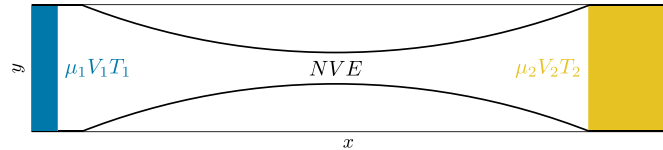


FIG. 2. Geometry of a slit Laval nozzle with the convergent and divergent part in the xy plane. The nozzle walls are two cylinders. In the z direction out of the plane, the nozzle is translationally invariant, realized with periodic boundary conditions. Particle insertion is done by grand-canonical Monte Carlo insertion and deletion [29,30] on the left side (blue), specifying chemical potential μ_1 , and temperature T_1 . The nozzle region shown in white with the convergent end divergent boundaries is simulated without Monte Carlo exchange and thermostat. Particle are deleted on the right side (yellow) by specifying μ_2 and T_2 .

walls would have significantly complicated the analysis of the flow, because of the nontrivial spatial dependence of the flow field in the direction perpendicular to the general flow direction, requiring significantly longer simulations to resolve all measured quantities in both the x and y directions. In a smooth-walled nozzle, we can restrict ourselves to studying only the x dependence of the quantities of interest.

The gas particles are atoms interacting via a pairwise Lennard-Jones (LJ) potential. Thus we simulate the expansion of a noble gas through the nozzle. Molecules with vibrational and rotational degrees of freedom seeded into the noble gas would be an interesting subject for further investigation, but this exceeds the scope of this work. The LJ potential between a pair of particles with distance r is given by

$$V_{\text{LJ}}(r) = 4\epsilon \left[\left(\frac{\sigma}{r} \right)^{12} - \left(\frac{\sigma}{r} \right)^6 \right]. \quad (3)$$

The smooth walls are also modelled via a LJ potential with

$$V_{\text{LJ}}(s) = 4\epsilon \left[\left(\frac{\sigma}{s} \right)^{12} - \left(\frac{\sigma}{s} \right)^6 \right], \quad (4)$$

where s is the normal distance between atom and wall. The repulsive part of the LJ potential make the walls impenetrable for the gas particles, and hence gas flows only through the constriction between the convex walls, while there are no particles on the concave outside part of the walls. For both the atom-atom and the atom-wall potential we use a cut-off radius of $r_c = 3\sigma$. A more realistic, but still smooth, wall potential would be the LJ potential integrated over an infinite half space leading to powers 3 and 9 of $\frac{\sigma}{r}$ [31–33]. This would be relevant when the atom-wall interaction is essential, such as for studies of wetting or other adsorption processes or of density oscillations of fluids near walls, but in the present case we only need the wall potential to provide the slit nozzle geometry, and therefore we chose the shorter-ranged LJ potential with powers 6 and 12.

We use the common reduced units for simulations of LJ particles if not otherwise stated; see Table I. Thus with the atom mass m , and the LJ parameters σ and ϵ for a specific noble gas, the results can be converted from reduced units to physical units.

Atoms are inserted and deleted in the inlet (blue) and outlet (yellow) by running the MD simulation in these regions as a

TABLE I. Conversion to dimensionless reduced units (*) used in this work.

Quantity	Reduced units
Distance	$x^* = x/\sigma$
Time	$t^* = t\sqrt{\frac{\epsilon}{m\sigma^2}}$
Energy	$E^* = E/\epsilon$
Velocity	$v^* = vt^*/\sigma$
Temperature	$T^* = Tk_B/\epsilon$
Pressure	$p^* = p\frac{\sigma^3}{\epsilon}$
Density	$\rho^* = \rho\sigma^3$

hybrid (GCMC) simulation [29], where we specify the chemical potential, the volume, and the temperature, (μ_1, V_1, T_1) and (μ_2, V_2, T_2) , respectively. A proper choice of these thermodynamic variables ensures that on average, an excess of particles are inserted in the inlet and particles are eliminated in the outlet, such that a stationary gas flow is established after equilibration. There are alternative insertion methods, such as the insertion-deletion method, where the mass flow is specified [34].

The temperature and chemical potential of the inlet reservoir is set to $T_1 = 2.0$ and $\mu_1 = -23$, which would correspond to a density $\rho_1 = 0.086$ and ensures that the pressure is not too high and the LJ particles remain in the gas phase. As mentioned above, the particle insertion region in the nozzle is not in equilibrium with a grand-canonical reservoir defining the (μ_1, V_1, T_1) ensemble, because the inlet volume is not closed on the side facing the nozzle. The outflow must be compensated by additional insertions, which makes the insertion rate higher than the elimination rate. Indeed, we observed that the average density in the insertion region is approximately half the density ρ_1 . Also the temperature in the inlet region is lower than the set value $T_1 = 2.0$. The resulting pressure in the insertion region is $p \approx 0.06$ in our reduced units. For argon with $\epsilon = 1.65 \times 10^{-21}$ J and $\sigma = 3.4$ Å [35] this translates to a temperature of $T = 179$ K and a pressure $p \approx 2.5 \times 10^6$ Pa in SI units. This is in the pressure range for molecular beam spectroscopy experiments [4].

The inlet conditions will converge to the specified reservoir variables if the number of GCMC moves is significantly larger than the number of MD moves or if the size of the inlet region is increased; both increase computational cost. Alternatively, the inlet conditions may be matched to the desired pressure and temperature by fine-tuning the reservoir variables and running many equilibration simulations, which again requires a high computational effort. In this work we refrain from perfectly controlling the thermodynamic state of the inlet although it leads to effectively different inlet conditions in differently sized nozzles.

In the convergent-divergent part of the nozzle, the atoms are propagated according to Newton's equation of motion, which would converge to the microcanonical ensemble if the nozzle were closed. Thus the MD trajectories are not biased by a thermostat nor Monte Carlo particle exchange, which can be crucial for dynamic studies [36] of nonequilibrium phenomena. Since we want to simulate expansion into vacuum, we simply set the pressure in the outlet to zero, such that particles entering the outlet region are deleted immediately.

For comparisons of different nozzle sizes, we scaled the slit nozzle in both x and y directions, while keeping the simulation box length z_{\max} in the translationally invariant z direction, perpendicular to the figure plane in Fig. 2, fixed. In the z direction, we apply periodic boundary conditions. We compared different simulation box lengths z_{\max} in the z direction to quantify unwanted finite-size effects in the z direction. Ideally, we want to keep z_{\max} larger than the mean free path. Especially for the dilute gas at the end of the divergent part, a sufficiently large z_{\max} is required to avoid such effects. For most simulations, we found $z_{\max} = 86.18\sigma$ or $z_{\max} = 43.09\sigma$ to be adequate, as shown below.

We initialize the NEMD simulations with particles only in the inlet region. Equilibration is achieved when the total number of particles in the simulation does not increase anymore but just fluctuates about an average value. When this steady state is reached, we start measurements by averaging velocities, pressure, density, etc.

The equilibrium equation of state for LJ particles is well known [37,38]. The equation of state is not needed for the MD simulations, but it is helpful for the analysis of the results, particularly for the calculation of the speed of sound and the Mach number. Specifying the Mach number, temperature, or pressure rests on the assumption of local thermodynamic equilibrium and thus on the validity of a local equation of state. In a microscopic nozzle, where the state variables of the LJ gas changes on a very small temporal and spatial scale, local thermodynamic equilibrium may be violated.

All simulations were done with the open-source MD software LAMMPS [39,40].

III. THERMODYNAMIC PROPERTIES

In this section we present thermodynamic results of our molecular dynamic simulations of the expansion through slit Laval nozzles: density, pressure, temperature, and Mach number. We check whether a microscopic nozzle exhibits the transition to supersonic flow and where the sonic horizon is located in nozzles of various sizes, and we compare to ideal gas continuum dynamics. The atomistic NEMD simulation also allows us to investigate if the gas attains a local equilibrium everywhere in the nozzle, with a well-defined temperature.

A. Very small nozzle

Figure 3 shows results for a very small Laval nozzle, with a throat width of only 3.9σ , i.e., only a few atoms wide. Figure 3(a) shows the nozzle geometry. The temperature is shown in Fig. 3(c). The kinetic temperature is the thermal motion of the atoms after the flow velocity at \mathbf{r} , $\mathbf{v}(\mathbf{r})$ is subtracted,

$$\frac{3}{2}k_B T = \sum_i \frac{m}{2} [\mathbf{v}_i - \mathbf{v}(\mathbf{r}_i)]^2. \quad (5)$$

Unlike in equilibrium, the temperature in a nonequilibrium situation such as stationary flow varies spatially, $T = T(\mathbf{r})$, provided that local equilibrium is fulfilled. If there is no local equilibrium, then there is no well-defined temperature. Although the right-hand side of Eq. (5) can still be evaluated, the notion of a "temperature" is meaningless if the thermal parts of the atom velocities do not follow a Maxwell-Boltzmann

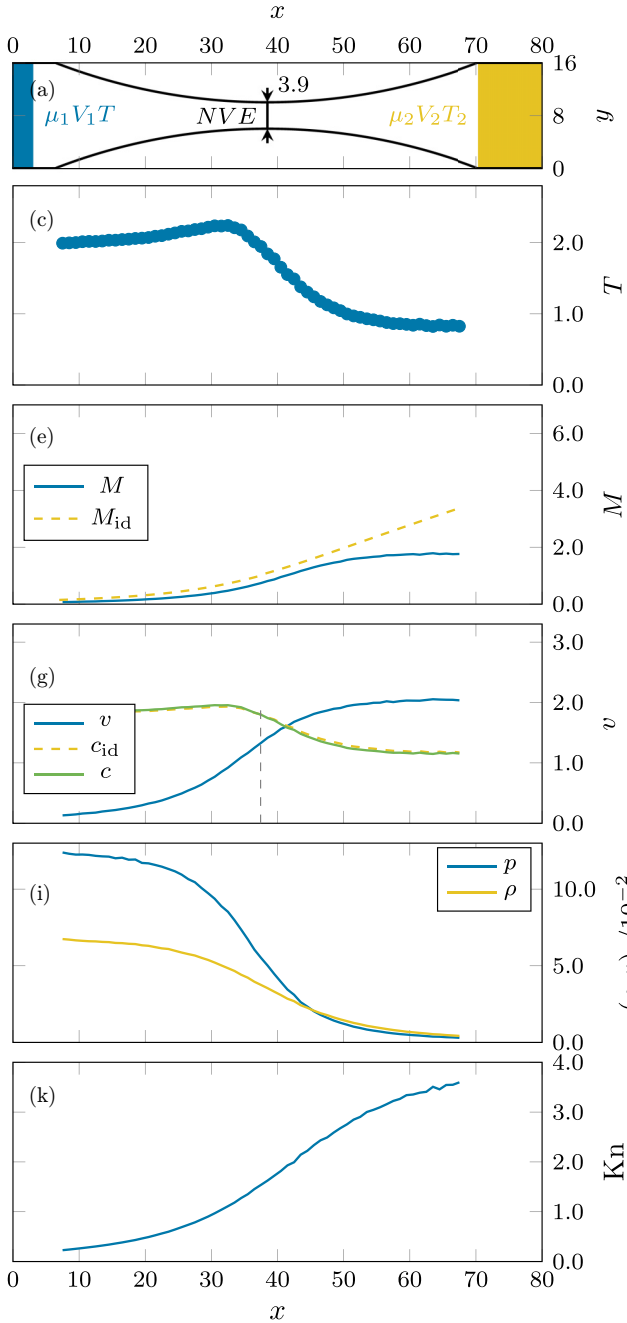


FIG. 3. Thermodynamic quantities for a nozzle with a throat width of only 3.9σ . The figure shows in panel (a) an overview of the nozzle in the $x - y$ plane; in (c) the temperature; in (e) the Mach number $M(x)$ and the ideal gas approximation for the Mach number M_{id} ; in (g) the ideal gas approximation of the speed of sound c_{id} , the speed of sound c obtained from the simulation and the averaged flow speed v ; in (i) the density ρ and pressure p ; and in (k) the Knudsen number. All quantities are shown as a function of the x position in the nozzle.

distribution. Here we assume that Eq. (5) provides a well-defined local temperature $T(x)$ at position x along the flow direction in our Laval nozzles. Further below we investigate whether this assumption is justified. The subtleties of the calculation of $\mathbf{v}(\mathbf{r})$ and $T(x)$, and how to subtract the

flow velocity from the particle velocities, can be found in Appendixes C and D, respectively.

Figure 3 shows that $T(x)$ indeed drops after the gas passes the nozzle throat, but there is a small increase before it reaches the throat. We attribute this to the wall potential: The constriction is dominated by the attractive well of the LJ potential (4). The associated drop in potential energy is accompanied by an increase of the temperature, i.e., kinetic energy.

Figure 3(g) shows the flow speed $v(x) = |\mathbf{v}(x)|$. $v(x)$ increases monotonously over the whole length of the nozzle. For comparisons, we also show the speed of sound of the LJ gas $c(x)$ and of the ideal gas $c_{id}(x)$, which are very similar, even in the convergent part where the density is higher. For a monatomic ideal gas, the speed of sound (2) becomes

$$c_{id}(x) = \sqrt{\frac{5}{3}k_B T(x)/m}. \quad (6)$$

The speed of sound $c(x)$ of the LJ fluid is calculated from its equation of state given in Ref. [37] and the specific residual heat capacities [38], using the expression with the isothermal derivative in Eq. (2) and the values of $\rho(x)$ and $T(x)$ measured in the MD nozzle simulations; $\rho(x)$ is shown in Fig. 3(i), together with the pressure. The heat capacities c_p and c_v appearing in Eq. (2) are also obtained from the equation of state of the LJ fluid. Note that applying the equation of state at position x in the nozzle again assumes local equilibrium, which is not necessarily true.

Figure 3(e) shows the Mach number $M(x)$ obtained from the simulation and the Mach number $M_{id}(x)$ for an ideal gas continuum. For the ideal gas, we can derive from Eq. (1) a relation between the cross-section areas $A(x)$ and Mach numbers $M_{id}(x)$ at two different positions x_1 and x_2 in the nozzle [10],

$$\frac{A(x_1)}{A(x_2)} = \frac{M_{id}(x_2)}{M_{id}(x_1)} \left[\frac{1 + \frac{\gamma-1}{2} M_{id}^2(x_1)}{1 + \frac{\gamma-1}{2} M_{id}^2(x_2)} \right]^{\frac{\gamma+1}{2(\gamma-1)}}. \quad (7)$$

$M_{id}(x)$ can now be obtained by setting $x_1 = x$ and $x_2 = x_c$, the position of the sonic horizon, where $M_{id}(x_c) = 1$ by definition. Figure 3(e) shows that the Mach number $M(x)$ obtained from the simulation stays below the ideal gas approximation $M_{id}(x)$, with the difference growing in the divergent part of the nozzle. At the end of the nozzle M is approximately half the value of the ideal gas continuum approximation M_{id} . In particular, the sonic horizon predicted by the MD simulation is located *after* the throat of the nozzle, not at the point of smallest cross section predicted by the continuum description of isentropic flow; see Eq. (1).

In the limit of vanishing density, $\rho\sigma^3 \rightarrow 0$, LJ particles approximately follow free paths between interactions with other particles. Especially near the inlet, these conditions are not really fulfilled; nonetheless, λ is a convenient phenomenological quantity to characterize the gas. In combination with flow through in narrow geometries, another phenomenological quantity is commonly used to characterize the flow, the Knudsen number, Kn . It is the mean-free-path length λ divided by a characteristic length d of confinement,

$$\text{Kn}(x) = \frac{\lambda(x)}{d(x)}. \quad (8)$$

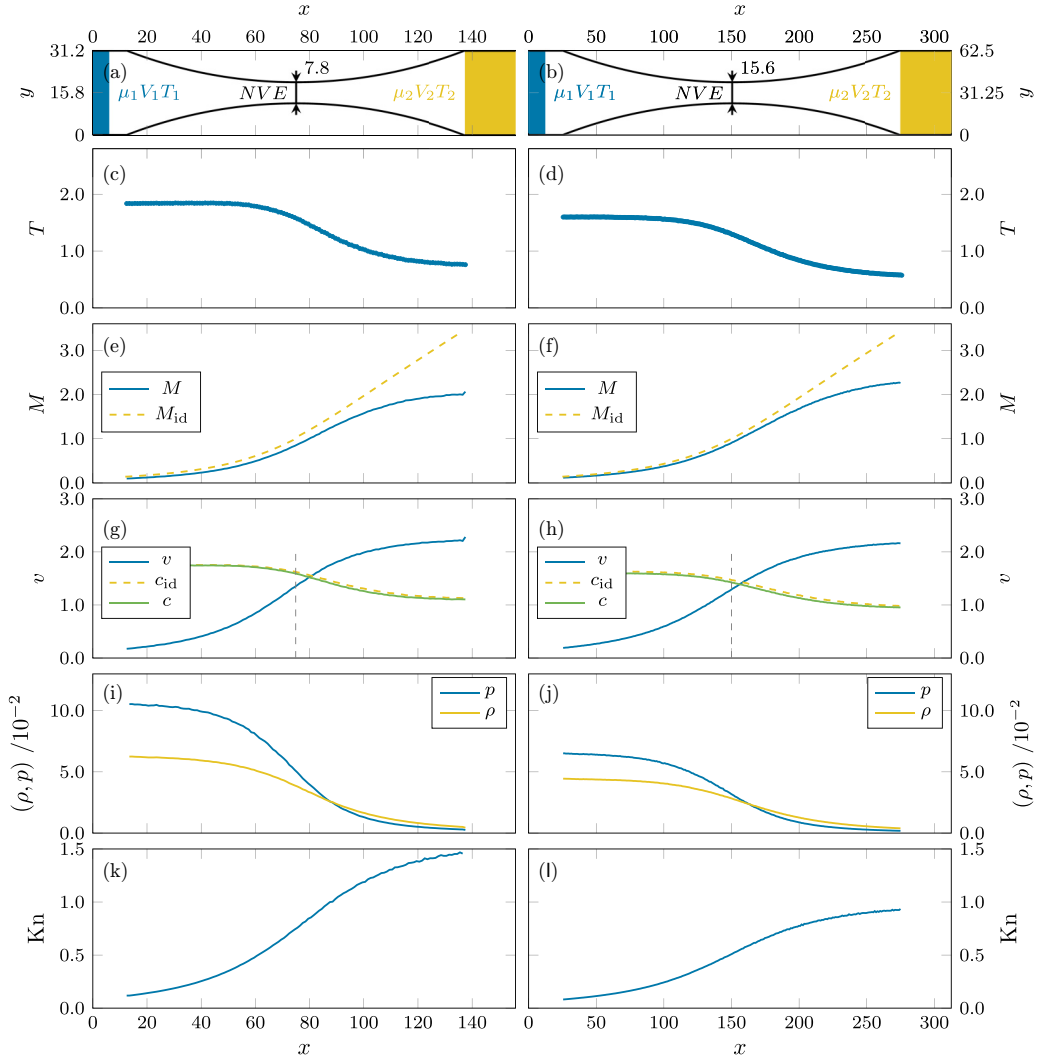


FIG. 4. Same as Fig. 3 for a throat width of 7.8σ (left column) and 15.6σ (right column).

In our slit Laval nozzle $d(x)$ is the width at position x and $\lambda(x)$ is the mean free path at position x . We estimate $\lambda(x)$ using the hard-sphere approximation [41]

$$\lambda(x) = [\sqrt{2}\pi\sigma^2\rho(x)]^{-1} \quad (9)$$

under the assumption of a Maxwell-Boltzmann distribution of the velocities which we check to be fulfilled in the nozzle; see Sec. IV A and Fig. 7. For $\text{Kn} \ll 1$ the mean free path is much smaller than the nozzle width and a continuum description of the flow is appropriate. For $\text{Kn} \approx 1$ or $\text{Kn} \gg 1$ a continuum description is not possible and the transport becomes partly ballistic. For the smallest nozzle results, the Knudsen number $\text{Kn}(x)$ shown in Fig. 3(k), is significantly larger than unity in the supersonic regime.

B. Small nozzles

Figure 4 shows results for two nozzles twice and four times as large as the smallest nozzle presented in Fig. 3, with throat widths 7.8σ and 15.6σ , respectively. The small temperature increase seen for the smallest nozzle is not present

anymore. T is almost constant in the convergent part and then decreases monotonously. Note that for each nozzle, the flow starts from slightly different thermodynamics conditions in the inlet region for reasons explained above. As the nozzle size increases, the Mach number M reaches a higher value for the larger nozzle despite the slightly lower T in the inlet, and it follows the ideal gas approximation M_{id} more closely. The sonic horizon moves closer to the minimum of the cross section. Of course the Knudsen number $\text{Kn}(x)$ is smaller for larger nozzles. Due to the wider nozzle throat, the pressure is significantly lower in the convergent part.

For Fig. 5, we increase the nozzle size again twofold and fourfold. We find the same trends as in Fig. 4. For the nozzle with throat width 62.5σ , the Mach number M is close to the ideal gas approximation M_{id} . M falls below M_{id} only towards the end of the nozzle, where the collision rate presumably becomes too low for efficient cooling. The sonic horizon is essentially in the center, indicated by the vertical dashed line.

For these two largest nozzles, we examined whether local equilibrium is fulfilled. The direction-dependent temperature, see Appendix D, is shown in Figs. 5(c) and 5(d). The

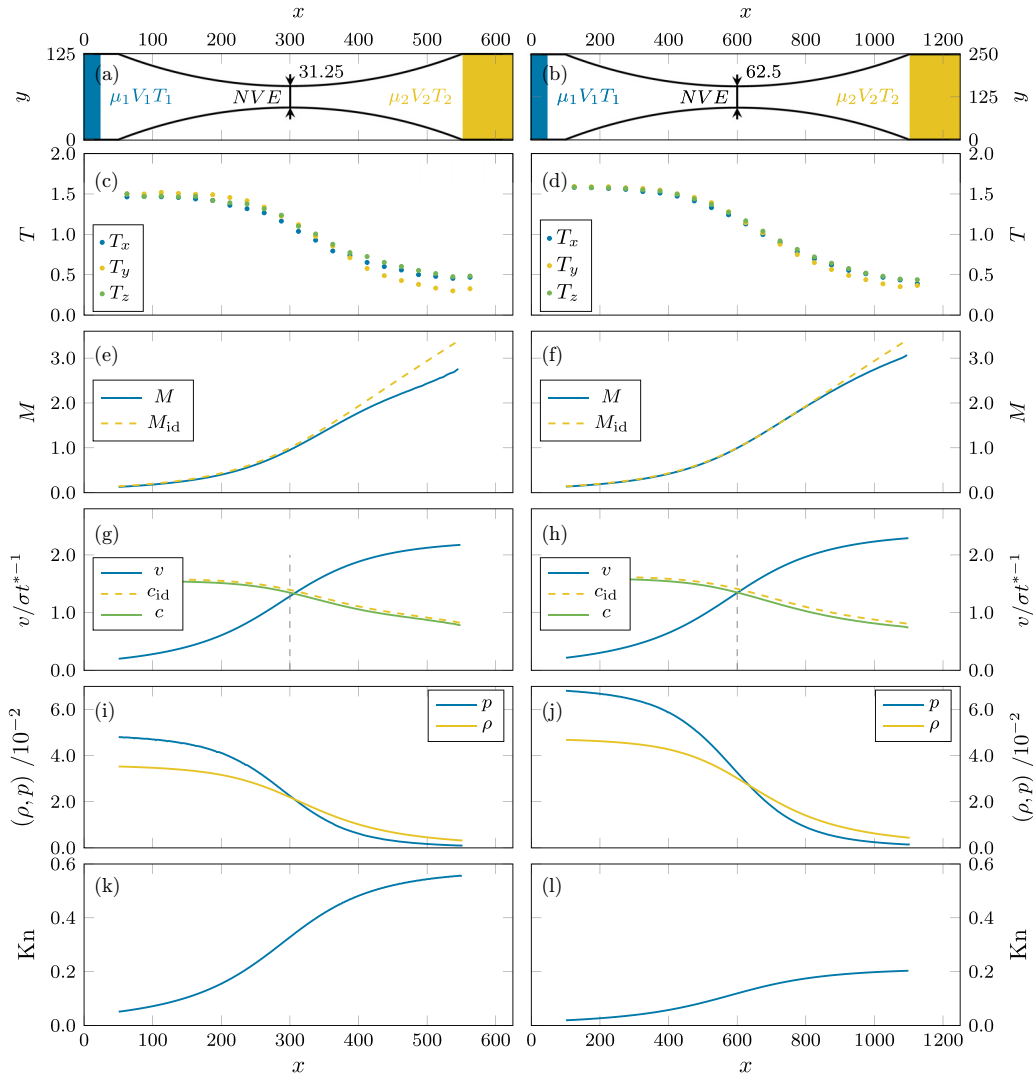


FIG. 5. Same as Fig. 3 for a throat width of 31.25σ (left column) and 62.5σ (right column). The temperature is split into its contribution from motion in the x , y , and z directions.

temperature is not quite isotropic, i.e., there is insufficient local equilibration between the motion in the x , y , and z directions. The three respective temperatures differ. In the convergent part the temperature in the y direction, T_y , is highest, while in the divergent part T_y is lower than T_x and T_z . T_z is only influenced by collisions between particles because there is no wall in the z direction. Comparing the two nozzles presented in Fig. 5, we observe the expected trend that the temperature anisotropy decreases with increasing nozzle size. At the end of the nozzles in Fig. 5 the temperature anisotropy grows because the collision rate between particles drops as the density drops. Whether the random particle velocities are Maxwell-Boltzmann distributed will be studied in Sec. IV about microscopic properties.

In Table II we compare the difference $\Delta x_c = x_c - x_c^0$ between the calculated position x_c of the sonic horizon and the position x_c^0 of minimal cross-section area predicted by isentropic flow in the continuum description. In all cases the sonic horizon is “delayed” and shifted downstream, $\Delta x_c > 0$. With growing nozzle size characterized by the throat width d_m , the dimensionless difference falls in relation to the nozzle

size, quantified by the ratio $\frac{\Delta x_c}{d_m}$ shown in the right column. In absolute numbers, Δx_c grows with size (middle column), until it actually drops for the largest nozzle.

Our atomistic simulations indicate that for a sufficiently large, but still microscopic, nozzle the sonic horizon is situated, with atomistic precision, in the middle, most narrow, position of the nozzle. For example, for the nozzle with a

TABLE II. Downstream shift Δx_c of the sonic horizon with respect to the center position predicted by continuum fluid dynamics. Nozzle are characterized by the minimal width d_m . The right column shows the dimensionless difference in relation to nozzle size, $\frac{\Delta x_c}{d_m}$.

d_m	Δx_c	$\frac{\Delta x_c}{d_m}$
3.90	3.78	0.97
7.80	4.97	0.64
15.60	5.96	0.38
31.25	6.09	0.19
62.50	2.74	0.044

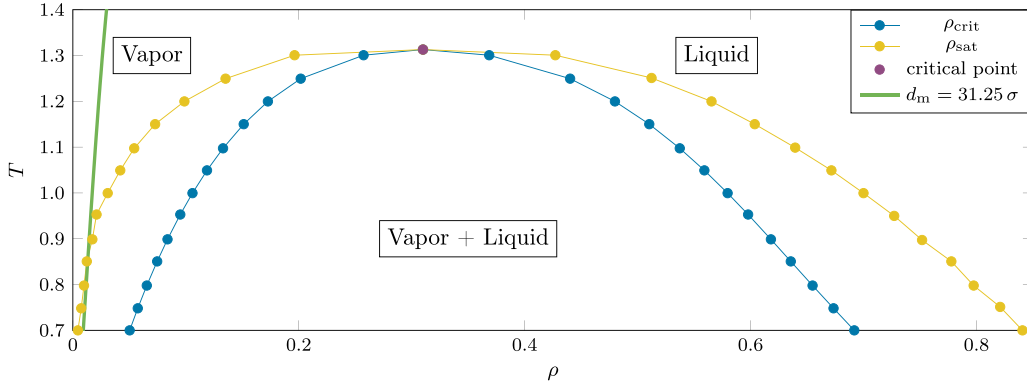


FIG. 6. Density-temperature phase diagram. Shown are the saturation density (yellow), the critical density (blue), and the critical point (purple) from the Lennard-Jones equation of state [37]. For the nozzle with a throat width $d_m = 31.25$, the path of temperature and density values are shown as a green curve.

throat width of 31.25σ , presented in the left panels of Fig. 5, the Knudsen number is $\text{Kn} \approx 0.3$ in the throat, i.e., the throat width is only three times larger than the mean-free-path estimate. Nevertheless, such a microscopic nozzle performs even quantitatively already in the same way as a macroscopic nozzle, at least for the present case of ideal, atomically flat walls, i.e., without boundary layer effect. Similar agreement with hydrodynamics, which after all is based on the assumption of local thermodynamic equilibrium, has been observed, e.g., for steady-state flow around a microscopic obstacle [18], but at much higher density than in this work. We find it surprising to find such agreement also for the transition to supersonic flow for the dilute conditions and the high acceleration in a microscopic Laval nozzle.

C. Phase diagram

Does the gas undergo a phase transition and condense into droplets at the end of the nozzle as it cools on expansion? Figure 6 shows the phase diagram of the LJ equation of state in the (T, ρ) plane as determined from Ref. [37]. The saturation density curve shown in yellow is associated with the phase transition, but up to the critical density, shown as blue curve, a supersaturated vapor phase or a superheated liquid phase is possible. This supersaturated and superheated phases are metastable. The green curve in Fig. 6 shows the path of density and temperature values, shown in Figs. 5(c) and 5(i), of the gas expansion in the nozzle with throat width $d_m = 31.25$. Strictly speaking, only an adiabatically slow evolution of a LJ fluid has a well-defined path in diagram Fig. 6, which shows *equilibrium* phases. But plotting the state during expanding through the microscopic nozzle in Fig. 6 at least provides a qualitative description of the fluid at a particular position in the nozzle. The path would extend to about $T = 0.4$, but the equation of state from Ref. [37] does not reach below $T = 0.7$. We note that the triple point, obtained from molecular simulations studies in Ref. [42] lies at $T_{\text{tr}} = 0.661$, below which the gas-liquid coexistence region becomes a gas-solid coexistence region.

From the path traced by the expanding gas we see that the LJ fluid starts in the gas phase in the inlet. As temperature and density fall on expansion, the fluid enters the gas-liquid

coexistence region. In this region the fluid can remain in a metastable supersaturated gas phase. Below the triple point, even the gas-solid coexistence region is reached at the end of the nozzle.

Our simulations show no evidence of a liquid or even a solid phase in our simulations, which would appear as small liquid or solid clusters; the LJ particles remain unbound until reaching the outlet region of the nozzle. Either the gas remains metastable or it is too far out of local thermal equilibrium that the discussion in terms of the phase diagram is meaningless. The anisotropy of the temperature discussed in the previous section indicates that thermal equilibrium is not completely fulfilled. The absence of nucleation of clusters is not a surprise, because there is simply not enough time in a microscopic nozzle for nucleation under such dilute conditions before the gas reaches the outlet.

IV. MICROSCOPIC PROPERTIES

Molecular dynamics simulation allows to measure properties which are inaccessible in a macroscopic continuum mechanical description. We already have seen in the previous section the temperature is slightly anisotropic, which is inconsistent with local equilibrium. In this section we take a closer look at quantities defined on an atomistic level: the velocity probability distribution (in equilibrium the Maxwell-Boltzmann distribution) and the velocity autocorrelation function. Furthermore, we study the propagation of density waves by calculating the upstream and downstream time correlations of thermal density fluctuations of the stationary flow before, at, and after the sonic horizon. The goal is to check if the sonic horizon, found in the previous section by thermodynamic consideration, is also a well-defined boundary for upstream information propagation on the microscopic level.

A. Velocity distribution

We have observed a temperature anisotropy; see Figs. 5(c) and 5(d). This raises the question whether the particle velocities even follow a Maxwell-Boltzmann distribution. If the velocities are not Maxwell-Boltzmann distributed, then we

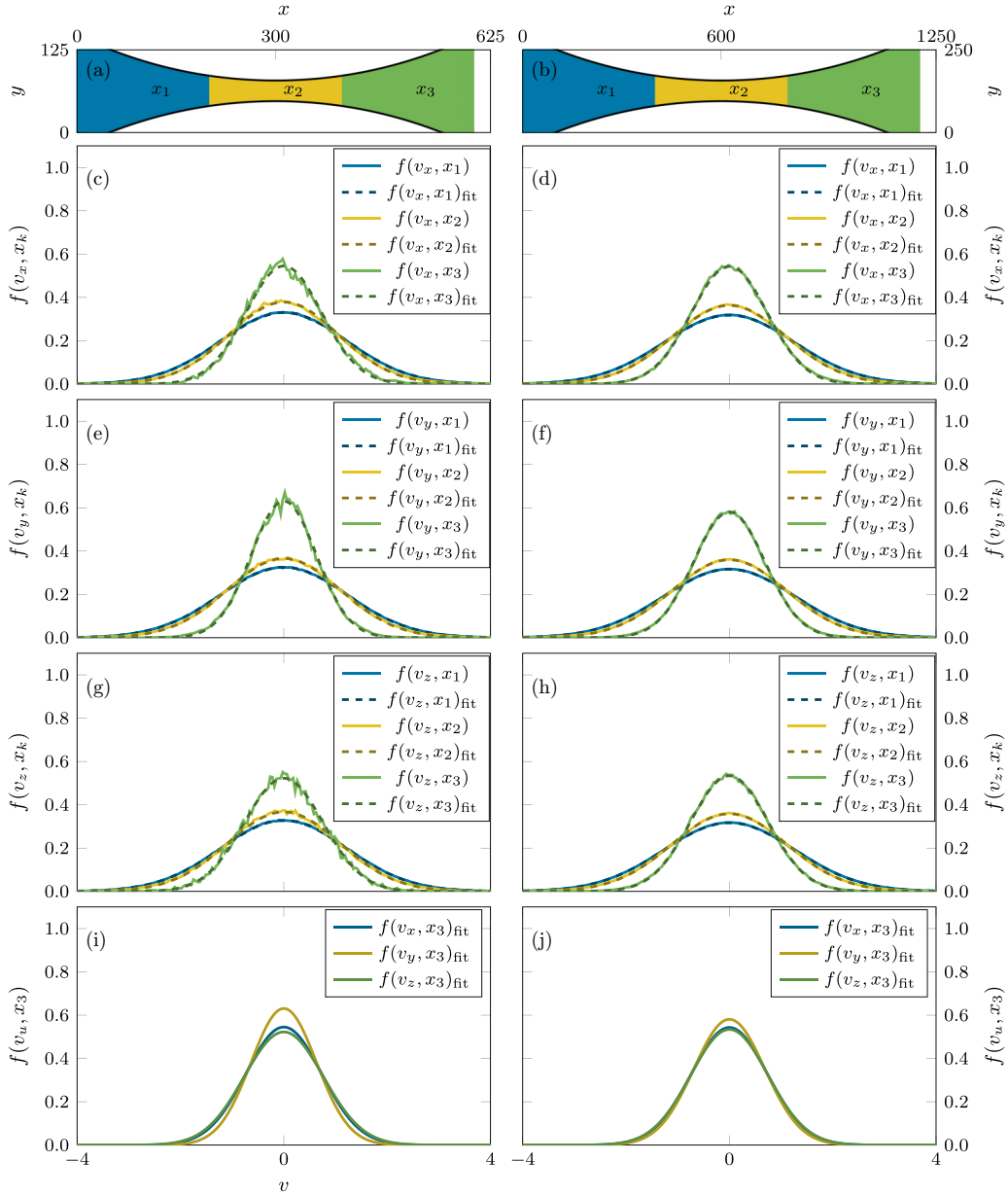


FIG. 7. Thermal part of the particle velocity distribution $f(v_i, x_j)$ for two nozzle sizes with a throat width of 31.25σ and 62.5σ in the left and right columns, respectively. Panels (a) and (b) show a schematic representation of those nozzles with the three regions x_1 , x_2 , and x_3 for which the velocity distributions are obtained from the MD simulations. Panels (c)–(h) show the velocity distribution of the components v_x , v_y , and v_z for the different regions in the nozzle. Also shown are Gaussian fits (dashed lines). Panel (i) and (j) are comparing the fits to the three velocity components in the x_3 region, in the diverging part of the nozzle.

do not have a well-defined kinetic temperature. This question is important for the interpretation of the results, for example when we discussed the temperature drop during expansion in the previous section. We now clarify whether it is meaningful to talk about temperature in microscopic nozzles.

We calculate the velocity distribution for the two largest nozzles (see Fig. 5) shown in Fig. 7 by separately sampling the histograms for the x , y , and z components of the velocity, where we subtract the steady flow velocity from the particle velocities; see Appendix D. Since the velocity distribution depends on the location x in the nozzle, the histograms are two dimensional, which requires a lot of data to sample from.

Therefore we split x into only three regions, x_1 , x_2 , and x_3 , depicted in the nozzle illustrations at the top of Fig. 7.

The velocity distributions $f(v_x, x_j)$ for the x component of the velocity are shown in Figs. 7(c) and 7(d) for the two respective nozzles, each panel showing $f(v_x, x_j)$ for all three regions $x_j = x_1, x_2, x_3$ in blue, yellow, and green. Of course, the distributions become more narrow for larger x_j , consistent with a downstream drop of temperature in a Laval nozzle. We fit the histograms with Gaussian functions, i.e., the Maxwell-Boltzmann distribution, also shown in the panels. The corresponding results $f(v_y, x_j)$ and $f(v_z, x_j)$ for the other two velocity directions are shown in Figs. 7(e)–7(h). It

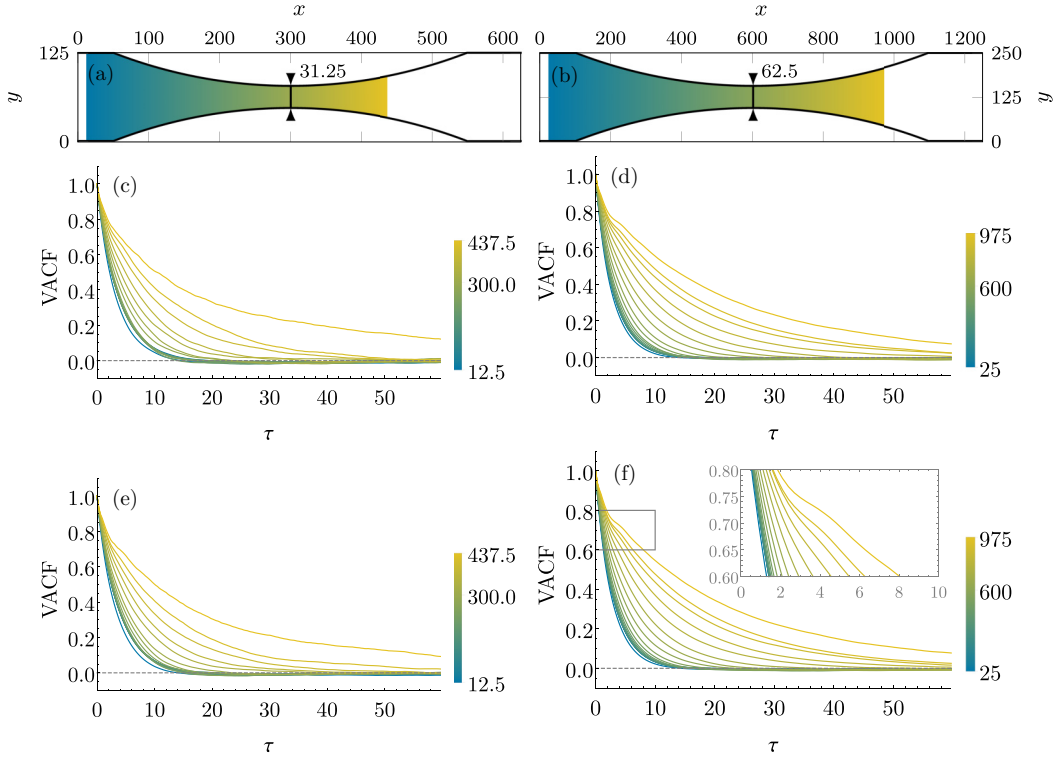


FIG. 8. Normalized velocity autocorrelation function $VACF(x, \tau)$ [Eq. (11)], along the nozzle with color-coded x position. Panels (a) and (b) show the shape and size of two nozzles, indicating the color scale for x in the panels below. Panels (c) and (d) show the VACF for nozzles with a distance $z_{\max} = 43.1\sigma$ between the periodic boundaries in the z direction. Panels (e) and (f) show the same for $z_{\max} = 86.2\sigma$. The inset of panel (f) shows a close-up of the shoulder around $\tau = 4$, discussed in the text.

is evident that, apart from small statistical fluctuations, the Maxwell-Boltzmann distribution is a good fit in all cases. Thus the notion of temperature in these microscopic nonequilibrium systems makes sense.

The width of the velocity distributions (i.e., the temperature) is not quite the same in the three directions, however; in particular in region x_3 , the diverging part of the nozzle. In order to see this better, we compare the fits to $f(v_i, x_3)$ for $i = x, y, z$ in Fig. 7(i) and 7(j). The distribution of the y component of the velocity is narrower than the other two directions. In other words the temperature according to v_y is lower, and thus the temperature is not isotropic. This means there is insufficient equilibration between the three translational degrees of freedoms. The effect is more pronounced for the smaller nozzle because particles undergo fewer collisions before they exit the nozzle, as quantified by the larger Knudsen number; see Fig. 5.

The spatial binning into just three region x_j is rather coarse-grained as it neglects the temperature variation within a region. With more simulation data a finer spatial resolution would be possible; however, we feel that the presented results are convincing enough that the thermal kinetic energy can be well characterized by a temperature, albeit slightly different in each direction.

B. Velocity autocorrelation function

The velocity autocorrelation function, VACF, quantifies the “memory” of particles about their velocity. The VACF is

defined as

$$VACF(\tau) = \langle \mathbf{v}_p(t) \cdot \mathbf{v}_p(t + \tau) \rangle_{t,p}, \quad (10)$$

where $\mathbf{v}_p(t)$ is the velocity of particle p at time t and $\langle \dots \rangle_{t,p}$ denotes an average over time and over all particles. An ideal, i.e., noninteracting, particle has eternal memory, $VACF_u(\tau) = \text{const}$. But due to interactions with the other particles, $VACF_u(\tau) \rightarrow 0$ within microscopically short times.

In the case of stationary flow, we need to subtract the flow velocity from particle velocities in Eq. (10). Furthermore, the VACF will depend on the x coordinate in the nozzle. Therefore we generalize Eq. (10) to a form which is suitable for stationary flow in a nozzle that depends on x and is not biased by the flow velocity. We also normalize the VACF such that it is unity at $\tau = 0$:

$$VACF(x, \tau) = \frac{\langle \Delta \mathbf{v}_p(t) \cdot \Delta \mathbf{v}_p(t + \tau) \delta(x - x_p(t)) \rangle_{t,p}}{\langle \Delta \mathbf{v}_p(t)^2 \delta(x - x_p(t)) \rangle}, \quad (11)$$

where $\Delta \mathbf{v}_p(t) \equiv \mathbf{v}_p(t) - \mathbf{v}(x_p(t))$ is the thermal part of the velocity, after subtraction of the flow velocity \mathbf{v} at the particle coordinate $x_p(t)$. Note that we define $VACF(x, \tau)$ such that the spatial coordinate x coincides with the starting point $x_p(t)$ at time t of the time correlation; at the final time $t + \tau$, the particle has moved to $x_p(t + \tau)$ downstream. When we sample (11) with a MD simulation, the coordinate x and the correlation time τ are discretized, and $\delta(x - x_p(t))$ is replaced by binning a histogram in the usual fashion; see the Appendix A.

Figure 8 shows the VACF for various positions x in the nozzle. The calculations were done for two different nozzle

sizes (left and right panels). The VACFs cannot be shown for x all the way to the end of the nozzles because particles leave the simulation before the velocity correlation can be evaluated. For example, if a particle in the smaller of the two nozzles in Fig. 8 is located at $x = 437$ at $\tau = 0$, then it will have moved with the flow on average to $x = 537$ at $\tau = 50$, where the outlet region starts and particles are removed from the simulation. For x close to the outlet, the VACF would be biased because the average in Eq. (11) would contain only particles which happen to travel slow, e.g., slower than the flow average.

The VACF decays monotonously for all x (in fact, the VACF for only the y component of the velocity (not shown) slightly overshoots to a negative correlations in the divergent part of the nozzle, which is a trivial effect of wall collisions). The decay is slower further downstream because the density drops. Towards the ends of the nozzles, the mean free path becomes large, see Fig. 5, reaching the length z_{\max} of the simulation box in z direction, where periodic boundary conditions are applied. We demonstrate that the finite-size bias in z direction is negligible by comparing the VACFs for different choices of z_{\max} . If z_{\max} were too small, then two particles might scatter at each other more than once due to the periodic boundaries, which would lead to a spurious oscillation in the VACF. Figures 8(e) and 8(f) show VACF(x, τ) for $z_{\max} = 86.2\sigma$, twice as large as in Figs. 8(c) and 8(d), corresponding to twice as many particles. Apart from the smaller statistical noise for larger z_{\max} , the VACFs for $z_{\max} = 43.1\sigma$ and $z_{\max} = 86.2\sigma$ are identical. This confirms that $z_{\max} = 43.1\sigma$ is large enough to obtain reliable results.

An interesting feature in the VACF for both nozzle sizes shown in Fig. 8 is a small shoulder around $\tau \approx 4$ in the divergent part, i.e., a small additional velocity correlation. The inset in Fig. 8(f) shows a close-up of the shoulder. Since this happens only at the low density in the divergent part of the nozzle, where the three-body collisions rate is low, the shoulder can be expected to be a two-body effect. It is consistent with pairs of particles orbiting around each other a few times. We test this conjecture by estimating the orbit period of two bound atoms in thermal equilibrium. The orbit speed v shall be determined by the temperature T . We further assume a circular stable orbit with diameter d . The orbiting particles have two rotational degrees of freedom, each of them related to the temperature T by

$$\frac{1}{2}k_B T = \frac{1}{2}mv^2. \quad (12)$$

The centrifugal force F_c and the attractive LJ force F_{LJ} must be balanced,

$$F_c + F_{LJ} = m \frac{2v^2}{d} - 4\epsilon \left(-12 \frac{\sigma^{12}}{d^{13}} + 6 \frac{\sigma^6}{d^7} \right) = 0. \quad (13)$$

The orbit period t_{rot} can now be calculated from Eq. (12) and Eq. (13),

$$t_{\text{rot}} = \pi \frac{d}{v} = \sqrt{\frac{m\sigma^2}{\epsilon}} \pi 6^{1/6} \left(\frac{\epsilon}{k_B T} \right)^{2/3} \left(1 - \sqrt{1 - \frac{2}{3} \frac{k_B T}{\epsilon}} \right)^{1/6}, \quad (14)$$

which expresses t_{rot} as function of the temperature. When we plug in a typical temperature towards the end of the nozzles of $T \approx 0.5$, we obtain an orbit time $t_{\text{rot}} \approx 5$, which is similar to the time when the shoulder in the VACF appears; see Fig. 8. This does not mean that bound dimers form in the supercooled flow near the exit of the nozzle, which requires three-body collisions. But the estimate based on bound states is applicable also to spiral-shaped scattering processes where two particles orbit each other a few times. Equation (14) is only a rough estimate of orbit periods, based only on circular orbits. But this estimated t_{rot} lies in the temporal range of the shoulder in Fig. 8, and hence the shoulder of the VACF of the expanding and cooling gas is in line with the picture of transient orbits of atoms pairs. Such scattering processes may be seeding events for the nucleation of van der Waals clusters and condensation in larger nozzles, but this question goes beyond the scope of the present work.

C. Density fluctuation correlations and the sonic horizon

The calculation of the speed of sound c according to Eq. (2), using the equation of state from Ref. [37], assumes local thermal equilibrium. However, the anisotropy of the temperature, see Fig. 5, shows that not all degrees of freedom are in local equilibrium during the fast expansion through a microscopic nozzle. Therefore, locating the sonic horizon may be biased by nonequilibrium effects. It is not even clear if a sonic horizon, the definition of which is based on macroscopic fluid dynamics, is microscopically well defined. While the thermal velocities of the atoms follow Maxwell-Boltzmann distributions, there are always particles in the tails of the distribution that travel upstream even after the sonic horizon. So maybe information can travel upstream on the microscopic scale of our nozzles, negating the existence of a sonic horizon.

The MD method provides the microscopic tools to answer this question by calculating space-time correlations of density fluctuations: If density fluctuations propagate upstream even in the divergent part of the nozzle, then there is no sonic horizon. We quantify the density fluctuation correlations before, at, and after the sonic horizon predicted from the calculation of the speed of sound. The instantaneous density $\rho(x, t)$ at position x and time t is evaluated according to Eq. (A2). The density fluctuation, i.e., the random deviation at time t from the average density at position x , is obtained by subtracting the time-averaged density (shown in Figs. 3–5) from $\rho(x, t)$, $\Delta\rho(x, t) = \rho(x, t) - \langle \rho(x, t) \rangle_t$. Note that fluctuations of the density depend also on y and z , but we are interested in the fluctuations relative the the sonic horizon, and thus fluctuations between different positions x in the nozzle. The correlation between a density fluctuation at x and t and a density fluctuation at $x + \delta x$ and $t + \tau$ is given by the time average,

$$S(\tau, x, \delta x) = \frac{\langle \Delta\rho(x, t) \Delta\rho(x + \delta x, t + \tau) \rangle_t}{\langle \Delta\rho(x, t) \Delta\rho(x, t) \rangle_t}, \quad (15)$$

where S is normalized such that it is unity for zero spatial and temporal shifts, $S(0, x, 0) = 1$.

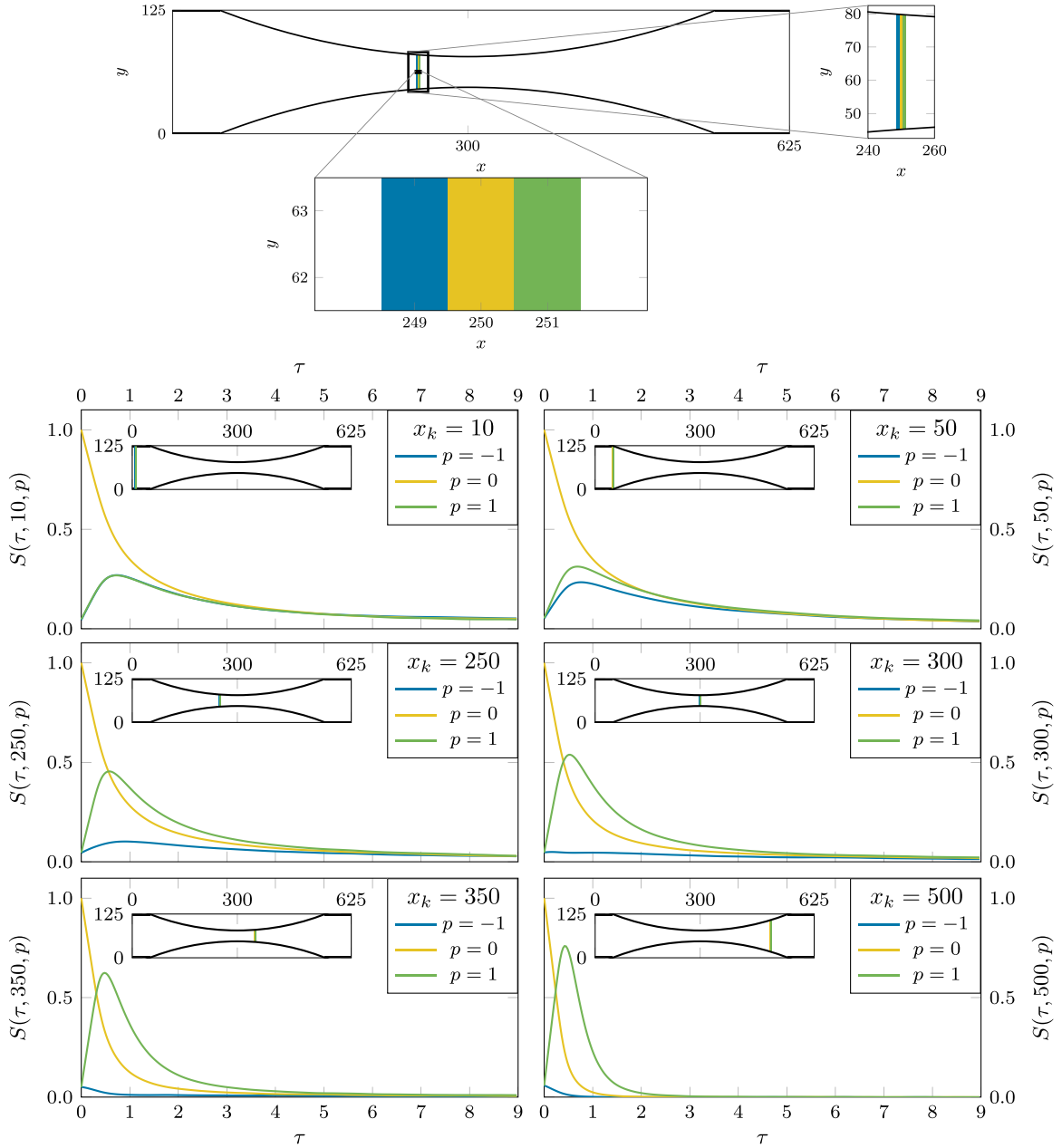


FIG. 9. Density fluctuation correlations $S(\tau, x, \delta x)$, Eq. (15). The panels show the self-correlation $S(\tau, x, 0)$ in yellow, a backward correlation $S(\tau, x, -\sigma)$ in blue and a forward correlation $S(\tau, x, \sigma)$ in green for different positions x in the nozzle as given in the insets. The illustration at the top shows the density bins used for calculating $S(\tau, x, \delta x)$: $S(\tau, x, 0)$ is obtained by correlating the yellow bin with itself, and $S(\tau, x, \sigma)$ or $S(\tau, x, -\sigma)$ are obtained by correlating the yellow bin with the green or blue bin, respectively.

In Fig. 9 we show the density fluctuation correlations $S(\tau, x, \delta x)$ in a nozzle with throat width 31.25σ , evaluated at six different positions x in the nozzle and for three relative position offsets $\delta x = p\sigma$ with $p \in \{-1, 0, 1\}$. The position x in the nozzle is indicated in an inset in each panel. The density binning, with bin size σ , is illustrated at the top of Fig. 9, which shows three adjacent bins at x , $x + \sigma$ and $x - \sigma$, corresponding to $p = -1, 0, 1$ in the figure labels.

The self-correlation $S(\tau, x, 0)$ (yellow curves), correlating only the temporal decay of the density correlations at x , is mainly influenced by the flow velocity and decays faster for

higher flow velocities because density fluctuations are transported away more quickly.

The upstream correlations $S(\tau, x, -\sigma)$ (blue curves) and the downstream correlations $S(\tau, x, \sigma)$ (green curves) are more interesting. Both correlations are small at zero delay time $\tau = 0$, because a density fluctuation at x needs some time to disperse to neighboring density bins. At position $x = 10$, where the flow speed is still small, there is no noticeable difference between upstream and downstream correlation. For larger x , hence for larger flow speed, the forward correlation increases and the backward correlation decreases, because the

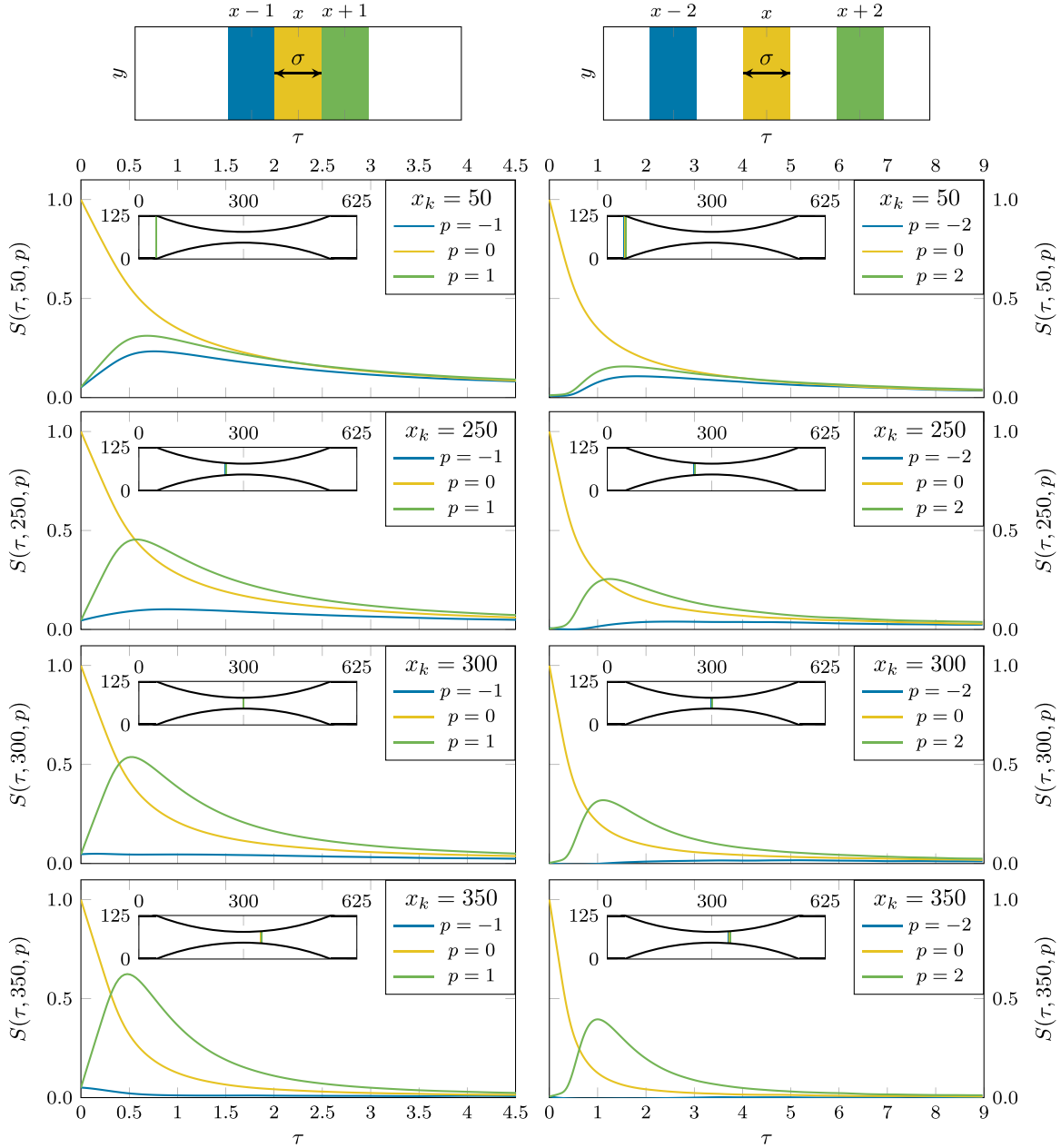


FIG. 10. Comparison of density fluctuation correlation $S(\tau, x, p\sigma)$ for different offsets, $p \in \{-1, 0, 1\}$ (left panels) and $p \in \{-2, 0, 2\}$ (right panels). At the top the respective binning is illustrated. In the insets the reference position x is indicated. The sonic horizon is situated slightly downstream of the nozzle throat ($x = 300$) at $x = 306$, according to the thermodynamic calculation of the local speed of sound.

density fluctuation disperses with the flow or against the flow, respectively.

According to the local speed of sound calculated in the previous section, see Table II, there is a sonic horizon at $x = 306$ for the nozzle size in Fig. 9. Indeed, for $x = 300$, the backward correlation has no peak anymore but decreases monotonously from a small nonzero value at $\tau = 0$. For even larger x , the upstream correlation decays more rapidly, yet it never completely vanishes at $t = 0$. The reason for this apparent contradiction to the existence of a sonic horizon is that the distance between bins and the width of the bins are both σ . The finite value at $\tau = 0$ is an artifact caused by the density

bins being directly adjacent to each other; see the illustration in Fig. 9: A density fluctuation at x will immediately have an effect on the adjacent bins at $x + \sigma$ and $x - \sigma$ since they share a boundary.

In order to remove this bias, we also calculated the correlations with offsets $\delta x = \pm 2\sigma$, $S(\tau, x, 2\sigma)$, and $S(\tau, x, -2\sigma)$, such that the upstream and downstream bins do not share a boundary with the bin at x . In Fig. 10 we compare the two choices of offsets. The left panels are taken from Fig. 9 where $\delta x \in \{-\sigma, 0, \sigma\}$; the right panels show $S(\tau, x, \delta x)$ with $\delta x \in \{-2\sigma, 0, 2\sigma\}$, with a twice-as-large τ range, because density fluctuations have to travel twice as far. The upstream

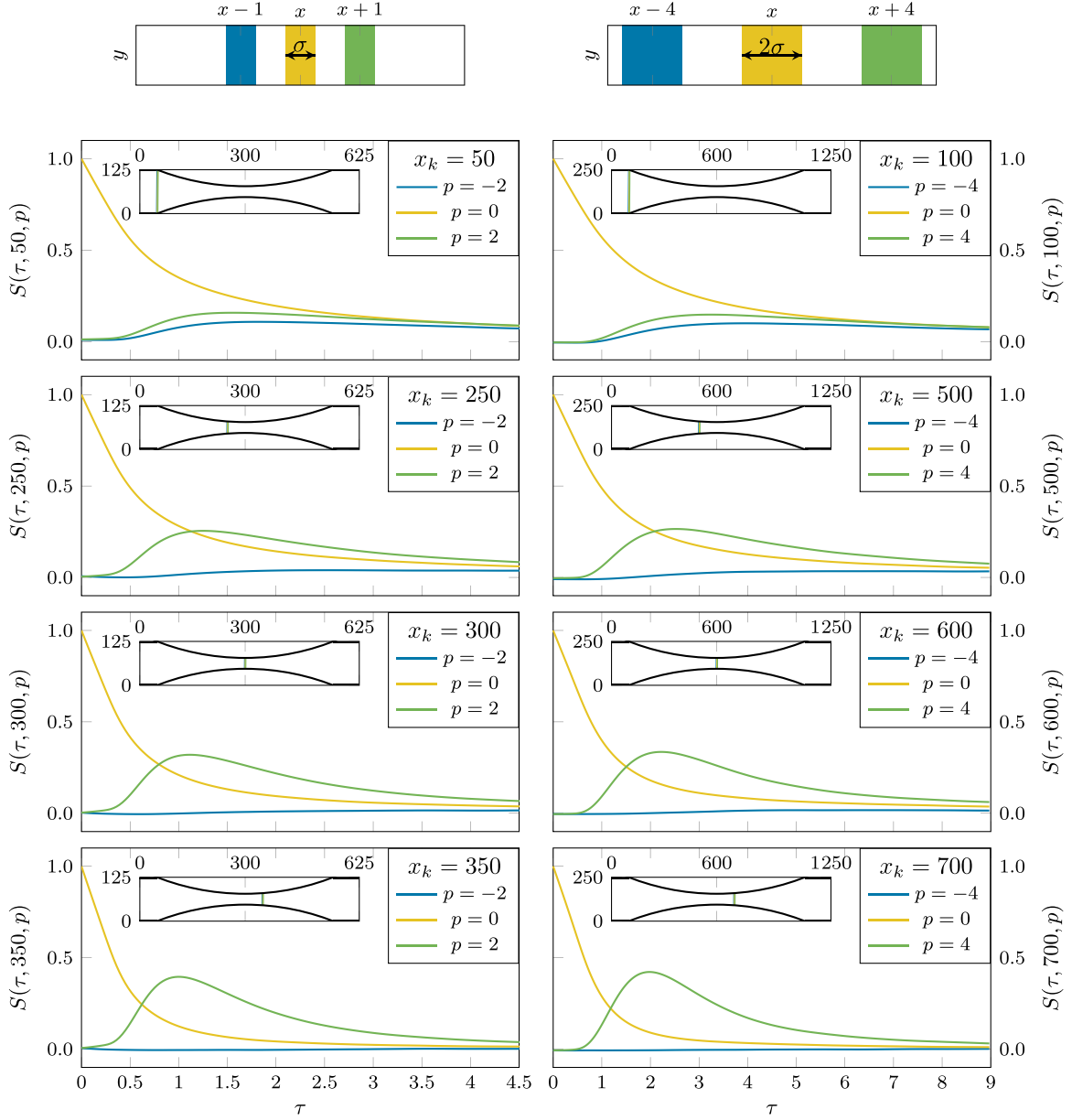


FIG. 11. Comparison of the density fluctuation correlations $S(\tau, x, \delta x)$ for two nozzle with throat width $d = 31.25\sigma$ (left panels) and $d = 62.5\sigma$ (right panels), respectively. All lengths are scaled by two for the larger nozzle, such that we compare the correlations for equal relative positions. At the top the density bin spacing is illustrated and the insets show the positions x .

and downstream correlations now vanish for zero time delay $\tau = 0$. The upstream correlation $S(\tau, x, -2\sigma)$ right at the throat at $x = 300\sigma$ is very small but does not quite vanish, which is consistent with a location of the sonic horizon predicted at $x = 306\sigma$ according to the speed of sound. Further downstream at $x = 350\sigma$, however, $S(\tau, x, -2\sigma)$ indeed vanishes within the error bars. This means that information about density fluctuations cannot travel backwards beyond the sonic horizon even on the microscopic scale of just a distance of 2σ . A microscopic Laval nozzle does have a sonic horizon.

We also calculated the density fluctuation correlations for a nozzle twice as large (length $L = 1250\sigma$ and throat width $d = 62.5\sigma$). Figure 11 compares the corresponding results

with those shown in Fig. 10. For the comparison, we scaled all lengths by two: The bins are 2σ wide, separated by 4σ ; see the illustration at the top of Fig. 11. We compare $S(\tau, x, \delta x)$ of the smaller nozzle with $S(2\tau, 2x, 2\delta x)$ of the larger one, i.e., at the same relative positions with the same relative upstream and downstream offset, and showing twice the time window for the larger nozzle. According to the speed of sound, the sonic horizon for the larger nozzle is located at $x = 603\sigma$ (see Table II), very close to the throat at $x = 600\sigma$. The comparison in Fig. 11 shows that the density fluctuation correlations are very similar for equal relative positions for both nozzles. Also for the larger nozzle, the correlations are very small at the throat. Further downstream at $x = 350\sigma$ and $x = 700\sigma$, respectively, both nozzles exhibit no upstream correlations.

Our calculations confirm that the thermodynamic determination of a sonic horizon, based on the equation of state, is valid, although the anisotropy of the temperature indicates that the rapid expansion through the nozzles hinder complete local thermal equilibrium. The location of the sonic horizon is consistent with the vanishing of upstream time correlations of density fluctuations. The existence of a microscopically narrow sonic horizon is a nontrivial result, considering the large estimated Knudsen numbers.

V. CONCLUSION

We studied the expansion of a gas of Lennard-Jones particles and its transition from subsonic to supersonic flow through microscopic Laval slit nozzles into vacuum. Our goal was to assess to what extent Laval nozzles with throat widths down to the scale of a few atom diameters still follow the same mechanisms as macroscopic nozzles where, given a sufficiently low outlet pressure, the gas flow becomes supersonic in the nozzle throat. For our study we used nonequilibrium MD simulations. MD is computationally demanding but makes the fewest approximations. We considered idealized nozzles with atomically flat surfaces with perfect slip to avoid boundary layer effects.

We introduced three thermodynamic regions for the nonequilibrium molecular dynamic simulation: an inlet region, the nozzle region, and the outlet region. In the inlet and outlet region, particle insertions and deletions are realized by grand-canonical Monte Carlo sampling [29]. After equilibration this allows to study stationary flows.

We obtained the thermodynamic state variables temperature, density, flow velocity, and pressure and their spatial dependence, as well as the Knudsen number, Mach number, velocity autocorrelation, and velocity distribution of the gas for nozzles of different sizes. We found a well-defined sonic horizon, i.e., the surface where the flow becomes supersonic, and analyzed it via space-time correlations of density fluctuations. We studied how the expansion dynamics depend on the nozzle size. Lower temperatures and correspondingly higher velocities and Mach numbers of the expanding gas are reached for larger nozzles, converging to predictions for isentropic expansion of an ideal gas continuum.

With nonequilibrium molecular dynamics we can observe phenomena which cannot be studied in continuum fluid dynamics, which assumes local thermodynamic equilibrium. We found that this assumption is violated for microscopic nozzles. The kinetic energy in the three translational degrees of freedom cannot equilibrate completely and is slightly different for each individual translational degree of freedom. The velocity components are still Maxwell-Boltzmann distributed, with a different width for each direction, which corresponds to an anisotropic temperature.

The LJ fluid in the inlet is in a vapor phase, but on expansion through the nozzle becomes supersaturated. At the end of the nozzle it is in the vapor-solid coexistence phase. Indeed, in the velocity autocorrelation function, VACF, we see indications of metastable pairs of particles. Since the expanding gas does not reach equilibrium in our microscopic nozzles, no clusters are formed. Cluster formation could be studied by enlarging the simulation and including the low

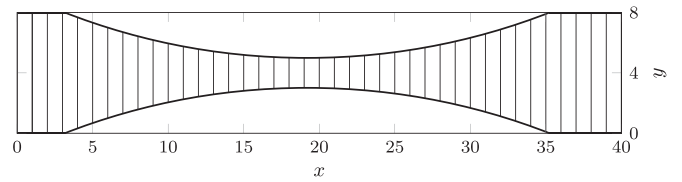


FIG. 12. Bin volumes of width σ used for calculating the density $\rho(x)$.

density region after the nozzle, giving the fluid enough time to equilibrate.

The investigation of the sonic horizon with the help of space-time-dependent correlations of density fluctuations showed that the position of the sonic horizon obtained from calculating the local speed of sound matches the position where density correlations practically cannot propagate against the flow. A microscopic distance on the order to the LJ particle size σ is already enough to completely suppress the backward correlations. The vanishing of backward time correlations does of course not happen abruptly at the sonic horizon; instead the backward correlations decrease gradually with the increasing flow velocity toward the sonic horizon. At the same time the forward correlations increase with the flow velocity. For larger microscopic nozzles, the simple macroscopic description relating the cross section to the Mach number is quite accurate. For smaller nozzles the position of the sonic horizon is shifted downstream.

In future work, it will be interesting to study nozzles with rough walls. The gas expansion through microscopic nozzles will be strongly affected by the boundary layer near the walls. Another topic of practical interest is the coexpansion of a carrier noble gas seeded with molecules to investigate the cooling efficiency of rotational and vibrational degrees of freedom of the molecules. This models the cooling of molecules for molecular beam spectroscopy. We note that nozzles for molecular beam spectroscopy are significantly larger than those studied here, with nozzle diameters of the order of tens of micrometers, instead of tenths of nanometers. Increasing the outlet region will allow to study not only the condensation of the gas into clusters but also the effect of a finite exit pressure on the position of the sonic horizon [13].

ACKNOWLEDGMENTS

We thank Stefan Pirker for inspiring discussions and the Scientific Computing Administration at Johannes Kepler University for the computational resources.

APPENDIX A: DENSITY CALCULATION

The density $\rho(x)$ as function of position x in the nozzle is calculated by binning the x coordinate of all particles. Since we are interested in stationary flow situations, we can take time averages of the number of particles in the bin of volume $V_{\text{bin}}(x)$. The binning volumes are slices, usually of thickness σ , which are centered at x , as illustrated in Fig. 12. This

average can be written as

$$\rho(x) = \left\langle \frac{1}{V_{\text{bin}}(x)} \sum_{i: p_i \in V_{\text{bin}}(x)} 1 \right\rangle_t \equiv \langle 1 \rangle_{t, V_{\text{bin}}(x)}, \quad (\text{A1})$$

with the sum counting all particles p_i in the volume of bin $V_{\text{bin}}(x)$ and the bracket denoting the time average. For calculations of space-time density correlations we need the instantaneous density at x at time t , which we obtain by omitting the time average in Eq. (A1),

$$\rho(x, t) = \frac{1}{V_{\text{bin}}(x)} \sum_{i: p_i \in V_{\text{bin}}(x)} 1. \quad (\text{A2})$$

The determination of $V_{\text{bin}}(x)$ is not trivial, since the wall is not a well-defined hard boundary but realized by the LJ potential (4). Choosing $z = 0$ in Eq. (4) for the volume calculation would overestimate the real volume effectively available for the particles, because it neglects the thickness of the ‘‘skin’’ due to the finite value of σ . We determined that $z = 0.8\sigma$ is the most suitable choice in the following way: We simulated a small nozzle (the size depicted in Fig. 12) with a constriction so narrow that almost no particle pass through in the course of a simulation. The wall position z , and hence the effective volume $V_{\text{bin}}(x)$, is determined such that the density $\rho(x)$ in the left half of the nozzle, obtained from (A1), is constant as expected for an equilibrium simulation in a closed geometry. If the skin thickness were over- or underestimated, then we would obtain a density increase or decrease towards the constriction, respectively.

APPENDIX B: PRESSURE CALCULATION

The pressure is calculated from the diagonal elements of the stress tensor which is calculated for each individual particle i as [30,40]

$$S_{iab} = -m_i v_{ia} v_{ib} - \frac{1}{2} \sum_{\substack{j: p_j \in V_i \\ j \neq i}} (r_{ia} F_{ijb} - r_{ja} F_{ijb}) \quad (\text{B1})$$

where $a, b \in \{x, y, z\}$ are the Cartesian components. The first term is the ideal gas contribution and is biased by the collective flow speed. Since only the thermal motion should contribute to S_{iab} , the flow velocity must be subtracted from \vec{v}_i ; see Appendix C below for the calculation of the flow velocity. The second term is the virial contribution from the LJ interaction. The summation is over all particles j within r_c from particle i , where r_c is the cut-off radius of the LJ potential. This defines the cut-off volume V_i of particle i . r_{ia} is component $a \in \{x, y, z\}$ of the coordinate of particle i and F_{ijb} the component b of the force of the pairwise interaction between particle i and j . We calculate the pressure $p(x)$ at position x in the nozzle by averaging the diagonal elements of the stress tensor S_{iab} over all particles i within the bin volume $V_{\text{bin}}(x)$,

$$p(x) = - \left\langle \frac{\rho(x)}{3} (S_{ixx} + S_{iyy} + S_{izz}) \right\rangle_{t, V_{\text{bin}}(x)}, \quad (\text{B2})$$

where $\langle \rangle_{V_{\text{bin}}(x)}$ denotes the average over $V_{\text{bin}}(x)$. We also average over the three diagonal elements because we assume an isotropic stress tensor. Remembering that the temperature is not isotropic in the nozzle, the assumption of an isotropic

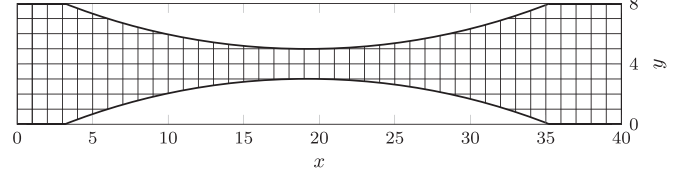


FIG. 13. Bin volumes $V_{\text{bin}}(x, y)$ with side length σ in the x and y directions.

stress tensor may not be valid. Inserting the stress tensor (B1) into the expression (B2) for the local pressure, we obtain

$$p(x) = \rho(x) k_B T(x) + \frac{1}{3} \left\langle \sum_{\substack{j: p_j \in [V_i \cap V_{\text{bin}}(x)] \\ j \neq i}} \mathbf{r}_i \mathbf{F}_{ij} \right\rangle_{t, V_{\text{bin}}(x)} + \frac{1}{6} \left\langle \sum_{\substack{j: p_j \in [V_i \setminus V_{\text{bin}}(x)] \\ j \neq i}} \mathbf{r}_j \mathbf{F}_{ji} \right\rangle_{t, V_{\text{bin}}(x)}, \quad (\text{B3})$$

where in the calculation of the local virial we have to distinguish between neighbor particles p_j which are also in the same binning volume $V_{\text{bin}}(x)$ as particle p_i (giving rise to the first virial expression with the common prefactor $\frac{1}{3}$) and those which are not (the second virial expression with the prefactor $\frac{1}{6}$). For the first virial expression we could use $\mathbf{F}_{ij} = -\mathbf{F}_{ji}$ and swap the summation index i and j leading to a factor 2. For the particles p_j which are not in volume $V_{\text{bin}}(x)$ this cannot be done, and each force \mathbf{F}_{ij} contributes just once.

APPENDIX C: CALCULATION OF VELOCITY

The velocity field $\mathbf{v}(x, y)$ in the nozzle depends on both the x and y coordinates. The velocity is not only a key quantity for Laval nozzles but also required for obtaining the temperature T , because $\mathbf{v}(x, y)$ needs to be subtracted from the particle velocities for the calculation of T ; see Appendix D. Figure 13 illustrates the bin volumes $V_{\text{bin}}(x, y)$ for the calculation of $\mathbf{v}(x, y)$, as opposed to the bin slices in Fig. 12. The time-averaged flow velocity \mathbf{v} in a bin volume $V_{\text{bin}}(x, y)$ can be calculated as

$$v_a(x, y) = \left\langle \frac{1}{N(x, y)} \sum_{i: p_i \in V_{\text{bin}}(x, y)} v_{ai} \right\rangle_t, \quad (\text{C1})$$

where $a \in \{x, y, z\}$, v_{ai} is the velocity component a of particle p_i , and $N(x, y)$ the number of particles in $V_{\text{bin}}(x, y)$ at a given time. The magnitude of the flow velocity is

$$v(x) = \sqrt{\langle v_x(x, y) \rangle_y^2 + \langle v_y(x, y) \rangle_y^2}. \quad (\text{C2})$$

On average there is no flow in the z direction, $v_z(x, y) = 0$.

APPENDIX D: TEMPERATURE CALCULATION

In order to investigate how the gas cools on expanding supersonically through the nozzle, we need to calculate the position-dependent temperature $T(x)$. The microscopic definition of the temperature is the kinetic energy of the *random* part of the particle velocity, hence we need to subtract the flow

velocity $\mathbf{v}(x, y)$ discussed in Appendix C:

$$k_B T(x, y) = m \left\langle \frac{1}{3N(x, y) - 3} \sum_{i: p_i \in V_{\text{bin}}(x, y)} [\mathbf{v}_i - \mathbf{v}(x, y)]^2 \right\rangle_t \quad (\text{D1})$$

We are interested only in the x dependence of the temperature and therefore we average over y ,

$$T(x) = \langle T(x, y) \rangle_y. \quad (\text{D2})$$

Note that subtracting the flow velocity removes three translational degrees of freedom, which we account for by

subtracting 3 from the number of degrees of freedom of the $N(x, y)$ particles in binning volume $V_{\text{bin}}(x, y)$.

In Eq. (D1) we average over the contribution of the three velocity components, which is fine in an isotropic system. In order to test whether the temperature is isotropic or not (and indeed we find it is not), we calculate the direction-dependent kinetic temperature,

$$k_B T_a(x, y) = m \left\langle \frac{1}{N(x, y) - 1} \sum_{i: p_i \in V_{\text{bin}}(x, y)} [v_{ia} - v_a(x, y)]^2 \right\rangle_t \quad (\text{D3})$$

where $a \in \{x, y, z\}$. Again, we are interested only in how T_a varies with position x along the nozzle, hence we average over y , $T_a(x) = \langle T_a(x, y) \rangle_y$.

-
- [1] W. G. Unruh, Experimental black-hole evaporation? *Phys. Rev. Lett.* **46**, 1351 (1981).
- [2] M. Visser, Acoustic black holes: Horizons, ergospheres and Hawking radiation, *Class. Quant. Grav.* **15**, 1767 (1998).
- [3] A. Kantrowitz and J. Grey, A high intensity source for the molecular beam. Part I. Theoretical, *Rev. Sci. Instrum.* **22**, 328 (1951).
- [4] P. S. H. Fitch, C. A. Haynam, and D. H. Levy, The fluorescence excitation spectrum of free base phthalocyanine cooled in a supersonic free jet, *J. Chem. Phys.* **73**, 1064 (1980).
- [5] R. E. Smalley, L. Wharton, and D. H. Levy, Molecular optical spectroscopy with supersonic beams and jets, *Acc. Chem. Res.* **10**, 139 (1977).
- [6] T. E. Gough, R. E. Miller, and G. Scoles, Infrared laser spectroscopy of molecular beams, *Appl. Phys. Lett.* **30**, 338 (1977).
- [7] A. R. Skinner and D. W. Chandler, Spectroscopy with supersonic jets, *Am. J. Phys.* **48**, 8 (1980).
- [8] M. V. Johnston, Supersonic jet expansions in analytical spectroscopy, *Trends Anal. Chem.* **3**, 58 (1984).
- [9] J. P. Toennies and A. F. Vilesov, Superfluid helium droplets: A uniquely cold nanomatrix for molecules and molecular complexes, *Ang. Chem. Int. Ed.* **43**, 2622 (2004).
- [10] G. Sanna and G. Tomassetti, *Introduction to Molecular Beams Gas Dynamics*, Vol. 226 (World Scientific, Singapore, 2005).
- [11] I. D. Boyd, P. F. Penko, D. L. Meissner, and K. J. Dewitt, Experimental and numerical investigations of low-density nozzle and plume flows of nitrogen, *AIAA J.* **30**, 2453 (1992).
- [12] H. Horisawa, F. Sawada, K. Onodera, and I. Funaki, Numerical simulation of micro-nozzle and micro-nozzle-array flowfield characteristics, *Vacuum* **83**, 52 (2008).
- [13] S. A. Saadati and E. Roohi, Detailed investigation of flow and thermal field in micro/nano nozzles using simplified bernoulli trial (SBT) collision scheme in DSMC, *Aerosp. Sci. Technol.* **46**, 236 (2015).
- [14] E. Roohi and S. Stefanov, Collision partner selection schemes in DSMC: From micro/nano flows to hypersonic flows, *Phys. Rep.* **656**, 1 (2016).
- [15] D. C. Rapaport, Microscale hydrodynamics: Discrete-particle simulation of evolving flow patterns, *Phys. Rev. A* **36**, 3288 (1987).
- [16] M. Moseler and U. Landman, Formation, stability, and breakup of nanojets, *Science* **289**, 1165 (2000).
- [17] K. Kadau, T. C. Germann, N. G. Hadjiconstantinou, P. S. Lomdahl, G. Dimonte, B. L. Holian, and B. J. Alder, Nanohydrodynamics simulations: An atomistic view of the Rayleigh–Taylor instability, *Proc. Natl. Acad. Sci. USA* **101**, 5851 (2004).
- [18] J. Horbach and S. Succi, Lattice Boltzmann versus molecular dynamics simulation of nanoscale hydrodynamic flows, *Phys. Rev. Lett.* **96**, 224503 (2006).
- [19] S. Yasuda and R. Yamamoto, Synchronized molecular-dynamics simulation via macroscopic heat and momentum transfer: An application to polymer lubrication, *Phys. Rev. X* **4**, 041011 (2014).
- [20] J. R. Bordin, J. S. Andrade, Jr., A. Diehl, and M. C. Barbosa, Enhanced flow of core-softened fluids through narrow nanotubes, *J. Chem. Phys.* **140**, 194504 (2014).
- [21] E. R. Smith, A molecular dynamics simulation of the turbulent Couette minimal flow unit, *Phys. Fluids* **27**, 115105 (2015).
- [22] H. Nowruzi and H. Ghassemi, Effects of nano-nozzles cross-sectional geometry on fluid flow: Molecular dynamic simulation, *J. Mech.* **34**, 667 (2018).
- [23] J. P. Toennies and A. F. Vilesov, Spectroscopy of atoms and molecules in liquid helium, *Annu. Rev. Phys. Chem.* **49**, 1 (1998).
- [24] G. Ciccotti, R. Kapral, and A. Sergi, Non-equilibrium molecular dynamics, in *Handbook of Materials Modeling*, edited by S. Yip (Springer, Dordrecht, 2005), pp. 745–761.
- [25] L. J. Garay, J. R. Anglin, J. I. Cirac, and P. Zoller, Sonic black holes in dilute Bose-Einstein condensates, *Phys. Rev. A* **63**, 023611 (2001).
- [26] J. Steinhauer, Measuring the entanglement of analogue Hawking radiation by the density-density correlation function, *Phys. Rev. D* **92**, 024043 (2015).
- [27] J. Steinhauer, Observation of thermal Hawking radiation and its entanglement in an analogue black hole, *Nat. Phys.* **12**, 959 (2016).
- [28] C. Barceló, S. Liberati, and M. Visser, Analogue gravity, *Living Rev. Relativ.* **14**, 3 (2011).
- [29] G. S. Heffelfinger and F. van Swol, Diffusion in Lennard-Jones fluids using dual control volume grand canonical molecular dynamics simulation (DCV-GCMD), *J. Chem. Phys.* **100**, 7548 (1994).

- [30] D. Frenkel and B. Smit, *Understanding Molecular Simulation: From Algorithms to Applications*, Vol. 1 (Academic Press, San Diego, CA, 2001).
- [31] F. Varnik, J. Baschnagel, and K. Binder, Molecular dynamics results on the pressure tensor of polymer films, *J. Chem. Phys.* **113**, 4444 (2000).
- [32] J. Baschnagel and F. Varnik, Computer simulations of supercooled polymer melts in the bulk and in confined geometry, *J. Phys.: Condens. Matter* **17**, R851 (2005).
- [33] E. Krotscheck and R. Zillich, Scattering of ^3He atoms from ^4He surfaces, *Phys. Rev. B* **58**, 5707 (1998).
- [34] P. L. Barclay and J. R. Lukes, Mass-flow-rate-controlled fluid flow in nanochannels by particle insertion and deletion, *Phys. Rev. E* **94**, 063303 (2016).
- [35] M. Griebel, T. Dornseifer, and T. Neunhoffer, *Numerical Simulation in Fluid Dynamics: A Practical Introduction*, Vol. 3 (SIAM, Philadelphia, PA, 1997).
- [36] R. Hafner, G. Guevara-Carrion, J. Vrabec, and P. Klein, Sampling the bulk viscosity of water with molecular dynamics simulation in the canonical ensemble, *J. Phys. Chem. B* **126**, 10172 (2022).
- [37] J. K. Johnson, J. A. Zollweg, and K. E. Gubbins, The Lennard-Jones equation of state revisited, *Mol. Phys.* **78**, 591 (1993).
- [38] D. Boda, T. Lukács, J. Liszi, and I. Szalai, The isochoric-, isobaric- and saturation-heat capacities of the Lennard-Jones fluid from equations of state and Monte Carlo simulations, *Fluid Phase Equilib.* **119**, 1 (1996).
- [39] S. Plimpton, Fast parallel algorithms for short-range molecular dynamics, *J. Comput. Phys.* **117**, 1 (1995).
- [40] A. P. Thompson, H. M. Aktulga, R. Berger, D. S. Bolintineanu, W. M. Brown, P. S. Crozier, P. J. in 't Veld, A. Kohlmeyer, S. G. Moore, T. D. Nguyen, R. Shan, M. J. Stevens, J. Tranchida, C. Trott, and S. J. Plimpton, LAMMPS - a flexible simulation tool for particle-based materials modeling at the atomic, meso, and continuum scales, *Comput. Phys. Commun.* **271**, 108171 (2022).
- [41] S. Chapman and T. G. Cowling, *The Mathematical Theory of Non-uniform Gases: An Account of the Kinetic Theory of Viscosity, Thermal Conduction and Diffusion in Gases* (Cambridge University Press, Cambridge, UK, 1970).
- [42] A. Ahmed and R. J. Sadus, Solid-liquid equilibria and triple points of n-6 Lennard-Jones fluids, *J. Chem. Phys.* **131**, 174504 (2009).